Article

Microstructure and Wear Resistance of Fe₃Al Coating on Grey Cast Iron Prepared via Direct Energy Deposition

Hossein Rajaei [1,*] , Sasan Amirabdollahian [2] , Cinzia Menapace [1] , Giovanni Straffelini [1] and Stefano Gialanella [1]

[1] Department of Industrial Engineering, University of Trento, Via Sommarive 9, 38123 Trento, Italy; cinzia.menapace@unitn.it (C.M.); giovanni.straffelini@unitn.it (G.S.); stefano.gialanella@unitn.it (S.G.)

[2] ProM Facility, Trentino Sviluppo S.p.A., Via Fortunato Zeni, 8, 38068 Rovereto, Italy; sasan.amir@promfacility.eu

[*] Correspondence: hossein.rajaei@unitn.it

Abstract: In this study, the potential of Fe₃Al coating material as an environmentally friendly alternative to coatings containing critical elements for brake discs was investigated. A buffer layer of Cr–Mo steel (Ferro 55) that was about 500 μm thick was applied on a gray cast iron disc to enhance the coating quality and prevent the formation of hot cracks during solidification. The microstructural analysis of the cross-section of the coating showed that the buffer layer diffused into the Fe₃Al coating, forming a combination of Fe₃Al, Fe, and Fe₃AlC₀.₅ phases. The tribological properties of the Fe₃Al-coated disc were evaluated using pin-on-disc tests against two different copper-free friction materials extracted from commercial brake pads. The wear results show a coefficient of friction comparable to that of an uncoated disc (≈0.55), but with a reduction in particulate matter (PM) emissions, which decreased from 600 to 476 #/cm³. The last issue is an interesting aspect that is gaining increasing importance in view of the upcoming international standards.

Keywords: DED; Fe₃Al; wear; Friction Coefficient (COF); emissions; brake disc

1. Introduction

Grey cast iron (GCI) has been extensively used in brake rotor applications due to its advantageous properties, which include outstanding castability, high thermal conductivity, good damping capability, cost-effectiveness, and adequate wear resistance. In fact, GCI is widely used as a rotor in brake systems for road vehicles. However, for this application, GCI still exhibits properties that are liable to be improved, like corrosion resistance and that it emits airborne particles [1,2].

In particular, the particles generated via the tribo-oxidation of GCI account for a significant fraction of particles released by braking systems [3] and are indeed the main source of airborne magnetite (Fe₃O₄) particles in urban areas [4]. The contribution of particulate matter emissions from disc brakes to pollution and their potential for emitting toxic components are two of the most serious environmental issues today [5]. New materials and technologies have been developed to address these concerns. For instance, carbon–ceramic composites have been established as an alternative to traditional brake disc materials since they display reduced wear rates and PM emission levels [6–8], However, because of the sophisticated production methods and unique features, these kinds of discs usually come with a higher price and are used for specific luxury cars. The application of coatings and disc surface treatments has also been investigated to reduce the wear and PM emissions of brake discs [2,9–12].

Coating GCI brake discs using direct energy deposition (DED) has proven to be an effective method, resulting in low-wear brake discs with increased durability and less particle emission [2,13,14]. As compared to the reference GCI samples [15], laser-cladded GCI brake discs with a Ni-self fluxing alloy and 60% spheroidized-fused WC exhibit higher

wear resistance and lower PM concentrations in PoD testing. However, harmful airborne particles are still released into the environment.

In this regard, intermetallic phase Fe$_3$Al exhibits promising characteristics. Fe$_3$Al is known for its low environmental impact, as it is composed of abundant non-toxic elements. Unlike certain coatings containing hazardous elements. like W, Ni, and Co [16–18], Fe$_3$Al eliminates the concerns associated with the release of harmful airborne particles. Additionally, Fe$_3$Al exhibits good corrosion resistance, making it an attractive choice for coating applications and for those applications requiring surface durability. These favorable qualities, combined with its relatively low cost and availability, place Fe$_3$Al as a desirable alternative to stainless steel and other materials in various industrial sectors [19,20]. Recently, the possibility of manufacturing Fe$_3$Al coatings on materials with lower corrosion resistance, such as low-alloy steel, has been investigated [21]. Comparing the wear resistance of iron aluminide alloys to that of other ceramics and metals, Alman et al.'s [22] research indicated that the resistance of iron aluminides was comparable to that of stainless steel.

Numerous studies have primarily focused on the application of this coating for improving the wear resistance of brake discs [11,12,15], frequently neglecting the critical environmental considerations associated with the selection of coating materials. Considering the promising characteristics of Fe$_3$Al and its potential as a coating material, this study aims to investigate the microstructure and wear resistance of an Fe$_3$Al coating on GCI prepared via DED. Using Fe$_3$Al powder, we intend to minimize the release of toxic elements into the environment and have the more general task of developing environmentally friendly brake systems with an enhanced performance and reduced environmental impact.

2. Materials and Methods

2.1. Materials

Gas-atomized, spherical Fe$_3$Al powder with a D50 of approximately 90 µm was used as the initial raw material, which was supplied by NANOVAl company, Berlin, Germany. In Figure 1, the scanning electron microscope (SEM) micrographs of the powder and optical microscope (OM) cross-sectional view of the coating are shown. Based on the X-ray diffraction (XRD) analysis conducted on the initial powder (see Figure 2), the only phase detected was Fe$_3$Al. This is supported by energy dispersive X-ray spectroscopy (EDXS) investigations, which indicated that the composition of the powder lies inside the Fe$_3$Al phase range (Fe-13.5 wt.% Al). A buffer layer of the Cr–Mo steel coating material was considered for improving the coating quality and adhesion. The composition of the buffer layer material is given in Table 1.
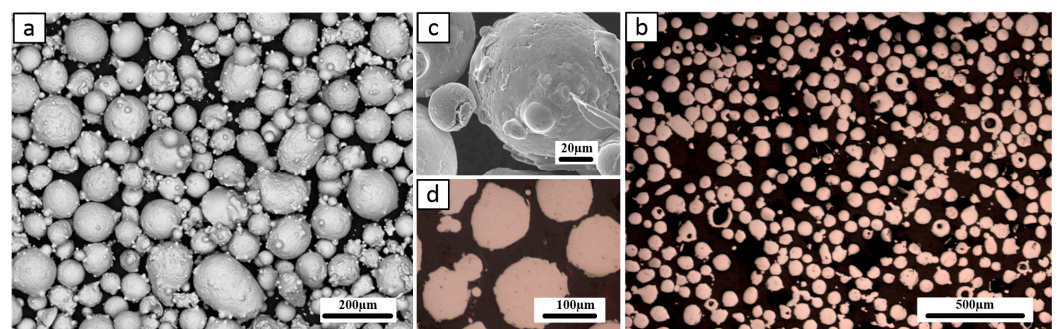

Figure 1. (**a**,**c**) SEM micrographs of gas-atomized Fe$_3$Al powder. (**b**,**d**) OM view of Fe$_3$Al powder cross-section.
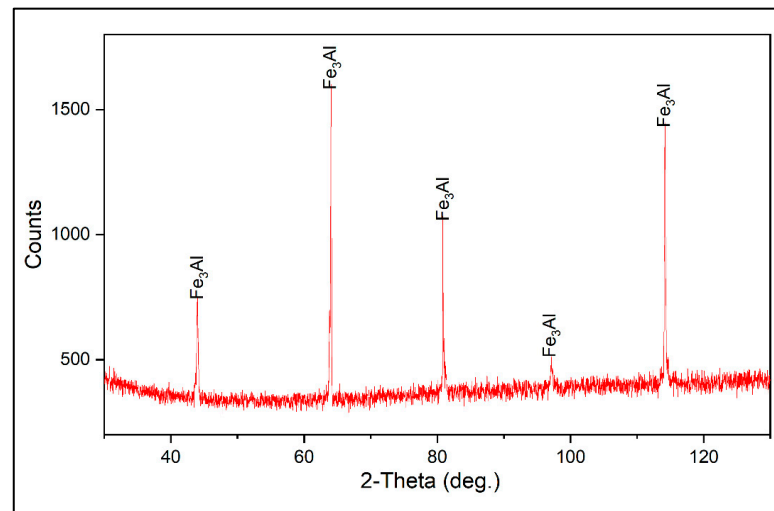
Figure 2. XRD pattern of the gas-atomized Fe$_3$Al powder.

Table 1. EDXS analysis of the Ferro 55 powder (wt.%).

	Fe	Cr	Mo	Mn	Si	C
Ferro 55	Bal.	7	2.2	1.1	0.3	0.35

2.2. Coating Deposition

For the deposition of the Fe$_3$Al coating, it is necessary to pre-heat the GCI substrate at temperatures higher than 150 °C in order to prevent defects and cracks generating in the coating structure. The deposition of a buffer layer prior to the deposition of the iron aluminide coating can provide enough energy for pre-heating the substrate and improving the bonding of the coating to the substrate. A buffer layer of Ferro 55 composition was deposited on the GCI disc right before the deposition of Fe$_3$Al coating (Table 2). After the buffer layer, the Fe$_3$Al coating was deposited at a scanning speed of 1000 mm/min, with a power of 1000 W and a powder feeding rate of 11 g/min (Figure 3).

An LASERTEC653D hybrid machine (DMGMORIAG, Bielefeld, Germany) with a 2500 W diode laser (=1020 nm) and a Coax14 powder nozzle was used to make for the deposition of the coatings. The laser had a focal length of 13 mm and a pot diameter of 3 mm with a top hat beam profile. The beam profile was shaped like a top hat.

Table 2. Compositions, from EDXS analyses, of the friction materials used in the pin on disc tests. Carbon was not considered in the quantification routine.

Elements (wt%)	Cu-Free	ECOPADS
O	26 ± 1	26 ± 1
Mg	8 ± 1	2.2 ± 0.5
Al	6.1 ± 0.2	1.6 ± 0.5
S	4 ± 1	7 ± 1
Si	3.4 ± 0.6	0.3 ± 0.6
Ca	5.1 ± 0.8	3.2 ± 0.3
Zn	12 ± 1	13.7 ± 0.8
Cr	2.5 ± 0.2	2 ± 0.4
Fe	28 ± 2	21 ± 4
Sn	8.1 ± 0.5	5.2 ± 0.5
Ba	-	21 ± 3

Figure 3. Fe_3Al coating with Ferro 55 buffer layer deposited on GCI substrate.

2.3. Wear Test

To assess the coating's tribological characteristics and to get an insight into the fundamental behavior of the coating sliding against the brake pad friction materials, a dry sliding pin-on-disc (PoD) test was performed. Two friction materials with different compositions were used to investigate the tribological behavior of the coating system. Cu-free and ECOPADS [23] friction materials were chosen as the pin materials (cylindrical shape), and their compositions, as indicated via EDXS analysis, are given in Table 2. For the PoD test, 14,400 m of the total sliding distance, a 2 m/s sliding speed, and 0.6 MPa of applied pressure were used. The selected PoD test conditions were intended to approximately simulate the mild wear condition, which is typical for braking systems [1,9,13]. The PoD test was also carried out on a GCI disc under identical testing conditions in order to provide a better reference point and an understanding of the coating properties comparatively. To avoid the initial surface roughness contributing to the final wear results, the same surface initial roughness Ra was taken into consideration for all the samples (approximately 0.25 μm).

Dry sliding wear tests were conducted using a Biceri PoD tribometer (Biceri, Leeds, UK) at room temperature following the ASTM G99 standard. Three trials were conducted for each combination of disc and friction materials. The assessment of wear resistance was pursued through the measurement of weight loss using a scale with an accuracy of ±0.1 mg. The height deviations of the pins were measured with a digital caliper, and subsequently, these data were used to calculate the wear rate.

2.4. Wear and Emission Measurements

The specific wear rate (K_a) was considered to compare how the different friction materials behaved when they slid against each other. The following formula (Equation (1)) is used to calculate K_a:

$$K_a = \Delta V / (S \times F_n) \tag{1}$$

where ΔV (m^3) is the wear volume measured after the wear test, F_n (N) is the applied load, and S (m) is the sliding distance.

The wear volume of the pin was estimated through the division of its weight reduction by its apparent density. To determine the wear area of individual discs, three measurements were conducted along the radial direction of the wear track using a profilometer instrument (model Hommel Tester T1000) (Hommelwerke GmbH, Villingen-Schwenningen, Germany), featuring a tip with a curvature radius of 5 μm. The scanning length on the disc was 12 mm with a scanning speed of 0.15 mm/s. The average wear volume of the discs was calculated using Equation (2):

$$\Delta V_{disc} = 2\pi r A \tag{2}$$

where r is the average wear radius, and A is the calculated wear area.

An Optical Particle Sizer (OPS) (TSI Incorporated, Shoreview, MN, USA) was used to measure the size of the emitted particles. With a sampling rate of 1Hz, the OPS instrument counts particles between 0.3 m and 10 m in size. As for the PM concentration, the OPS device can sample between 0 and 3000 particles/cm^3.

2.5. Characterization

The cladded layers underwent etching using a Nital solution with a concentration of 2%. The study involved the use of a JEOL IT 300 SEM, (JEOL Ltd., Akishima, Japan) with an EDXS system (EDXS; Bruker, Billerica, MA, USA) for semi-quantitative composition analyses to conduct microstructural observations of the coating and the worn surfaces of the pins and discs. The SEM was operated at an accelerating voltage of 20 kV.

The coated disc underwent XRD analyses in order to assess its phase composition. Data were collected with an Italstructures IPD3000 diffractometer (XRD, GNR Analytical Instruments Group, Novara, Italy), which employed a Co Ka radiation source and an Inel CPS120 detector. The detector was able to simultaneously capture the signal over an angular span ranging from 5° to 120°.

The microhardness of the coatings was measured using a Future-Tech microhardness tester (FM-310) (Future-Tech Corporation, Kawasaki, Japan) on a polished cross-sectional sample. The assessment was conducted from the surface down to the GCI substrate, with a force load of 300 g and a 10 s indentation duration. The study on hardness was conducted in a sequential manner, commencing from the surface layer and progressing downwards, with a series of indentations spaced at regular intervals of 0.15 mm. The objective was to gain a comprehensive understanding of the variations in hardness across the various layers.

3. Results and Discussion

3.1. Coating Characterization

Figure 4 depicts a cross-section of the Fe$_3$Al coating (Fe$_3$Al coating with Ferro 55 Buffer layer), where the buffer layer of F55 was first deposited onto the GCI before the deposition of the Fe$_3$Al coating. The buffer layer was used to improve the coating quality by decreasing defects deriving from the interaction of the Fe$_3$Al coating with the GCI substrate during deposition and solidification.

Figure 4a shows a low-magnification view of the coating cross-section from the top to the bottom, which shows a defect-free coating microstructure, particularly at the substrate/buffer layer boundary. The microstructure of the Fe$_3$Al coating, as depicted in the cross-section of the coating near the surface in Figure 4b, reveals the presence of large grains with smaller needle-like structures dispersed throughout the material. These needle-like grains, as supported by the EDXS maps in Figure 5, appear to correspond to Fe-Al carbides. Figure 4c depicts the interface between the top coating and the buffer layer, revealing the significant diffusion of the buffer layer into the Fe$_3$Al coating, mainly along the grain boundaries. The outer parts of the coating are affected by diffusion from the substrate to a lower extent, showing smaller and less numerous needle-like grains.

Figure 5 shows X-ray element distribution maps acquired at the boundary region between the buffer layer and the Fe$_3$Al coating (magnified area in Figure 4c). This reveals that the Fe$_3$Al coating contains large carbon-enriched needle-like grains. These grains are Fe-Al carbides resulting from the diffusion of carbon from the buffer layer. Interestingly, the grain boundary of the coating has a higher concentration of chromium, confirming that the main pathway for the diffusion of carbon is the grain boundary region.
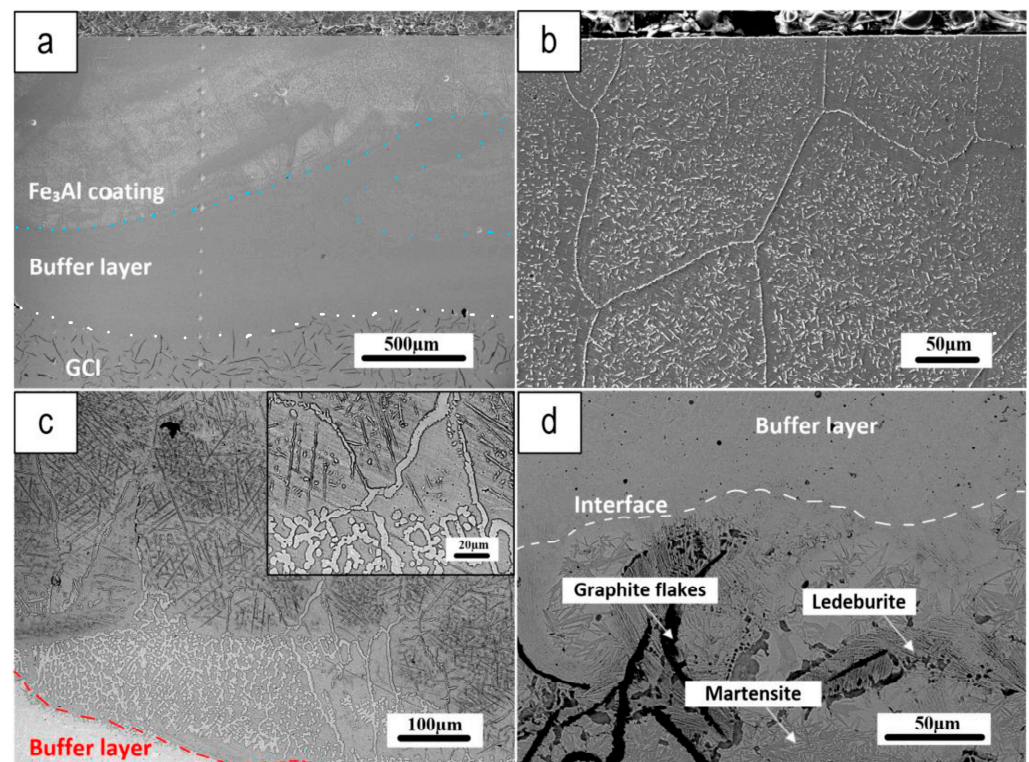
Figure 4. (**a**) Coating cross-section; (**b**) microstructure of the cross-section near the coating surface; (**c**) coating cross-section boundary between the top coating and F55 buffer layer, with a magnified view in the inset; and (**d**) coating cross-section border between the buffer layer and substrate.
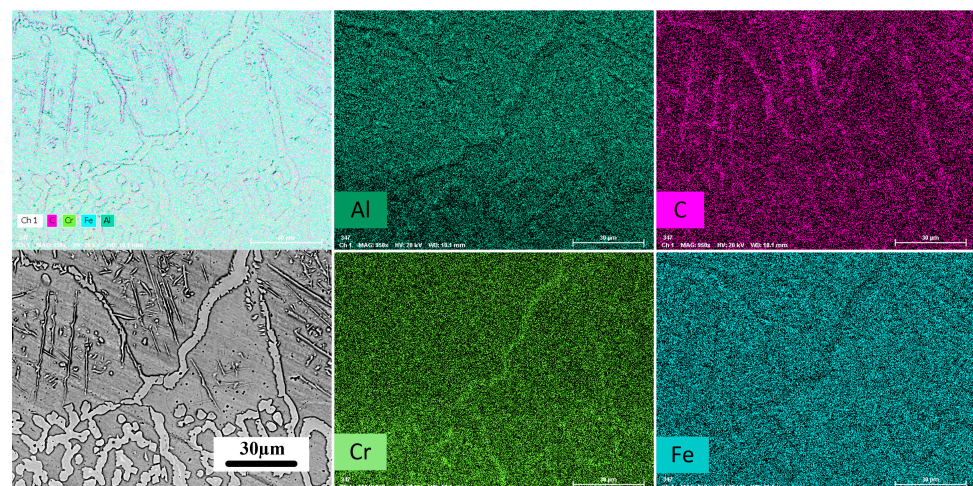

Figure 5. Color X-ray map of the cross section depicting the boundary between the Fe_3Al Coating and F55 buffer layer (refer to Figure 4c).

Figure 4d shows a high-resolution micrograph of the GCI microstructure near the interface with the buffer layer. A laser beam melts the F55 powder during deposition, with the residual heat partially melting the GCI, thus promoting the diffusion of carbon from the graphite flakes in the GCI. As the melt pool passes away, the rapid solidification of the GCI near the deposition boundary produces a martensitic structure. On the edge of the graphite flakes, there are also chilled ledeburite phases.

Grum and Sturm [24] observed the development of ledeburite shells around graphite in cast iron during laser surface remelting. They propose that the carbon-saturated iron surrounding the graphite flakes solidifies near the eutectic point. Because the higher temperatures in the Heat Affected Zone (HAZ) are near the border, carbon diffusion promotes the formation of broad regions of ledeburite along the coating–substrate interface. Figure 4d shows very good metallurgical bonding between the GCI and the buffer layer and the presence of a martensitic structure in the HAZ.

Figure 6 shows SEM images of the coating microstructure. Needle-like particles can be seen dispersed throughout the coating matrix. Figure 6a depicts a mixed area, the edge of which is outlined by a yellow dashed line, where buffer layer components diffused outward into the surface Fe_3Al coating, altering its typical microstructure. Figure 6b shows a higher magnification view of this mixed area close to the interface with Fe_3Al coating, indicating the difference between the grain size in this mixed area and the usual Fe_3Al microstructure (shown in high magnification in Figure 6c). This picture is confirmed by the analytical data. Figure 7a,b shows the EDXS results obtained from the pointed areas on the coating matrix and the needles, respectively (Figure 6), revealing that the elements from the buffer layer, such as Cr, C, and Si, have dissolved into the Fe_3Al coating. Furthermore, by comparing the intensities of the carbon in the matrix and needles (Figure 7a,b), it can be seen that the concentration of carbon in the needles is greater than that in the matrix (as was clearly shown in Figure 5 for the cross-section of this coating). The EDX spectrum in Figure 7c, referring to the mixed area (point C in Figure 6b), reveals the presence of relatively higher quantities of Fe and Cr and a smaller amount of Al in the mixed area. These findings indicate a significant diffusion from the buffer layer, mainly along grain boundaries toward the coating surface. In the literature, other researchers have demonstrated that Cr additions to Fe_3Al may have positive effects on mechanical properties, namely room temperature ductility and fracture toughness, which can be both improved significantly by chromium additions of up to 6% [25–27].
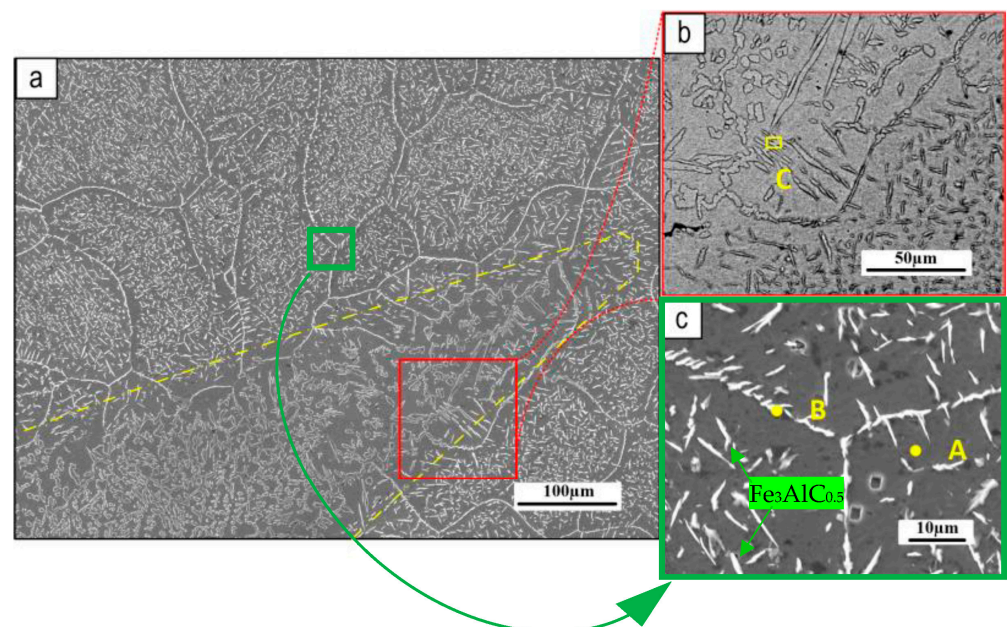

Figure 6. SEM of the Fe_3Al-coated surface: (**a**) general view; (**b**,**c**) higher-magnification images. The dotted line depicts a mixed area, in which the Fe_3Al is modified by the outer diffusion of elements from the buffer layer.
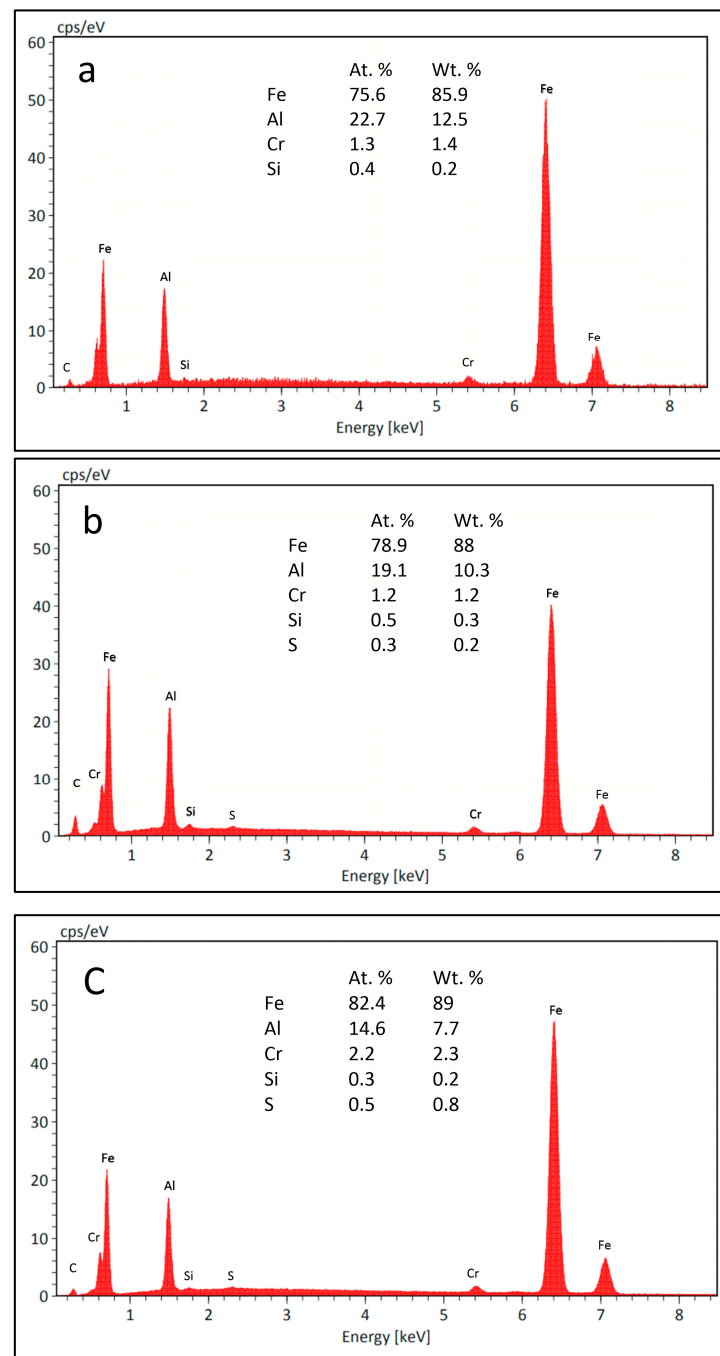
Figure 7. EDXS analysis of the defined areas in Figure 6; (**a**) matrix area "A", (**b**) needle-like grain "B", and (**c**) area "C".

Figure 8 shows the Vickers hardness profile of the Fe_3Al coating. This profile was collected at the center of the sample away from the edges (i.e., the first and last deposition tracks). The hardness of the Fe_3Al coating is between 310 and 350 HV0.3. However, it rises sharply in the F55 buffer layer to roughly 650–690 HV0.3, a typical hardness value for an F55 coating. The hardness of the HAZ also reaches to this range, after passing it through the GCI substrate, the hardness drops below 300 HV0.3.

The existing phases in the Fe_3Al coating were also identified using XRD analysis (Figure 9). The main detected phases are Fe_3Al, $Fe_3AlC_{0.5}$, and Fe. According to the XRD results, the formation of the $Fe_3AlC_{0.5}$ phase is a further consequence of the reaction of the matrix with the diffused and dissolved carbon from the bottom layer.

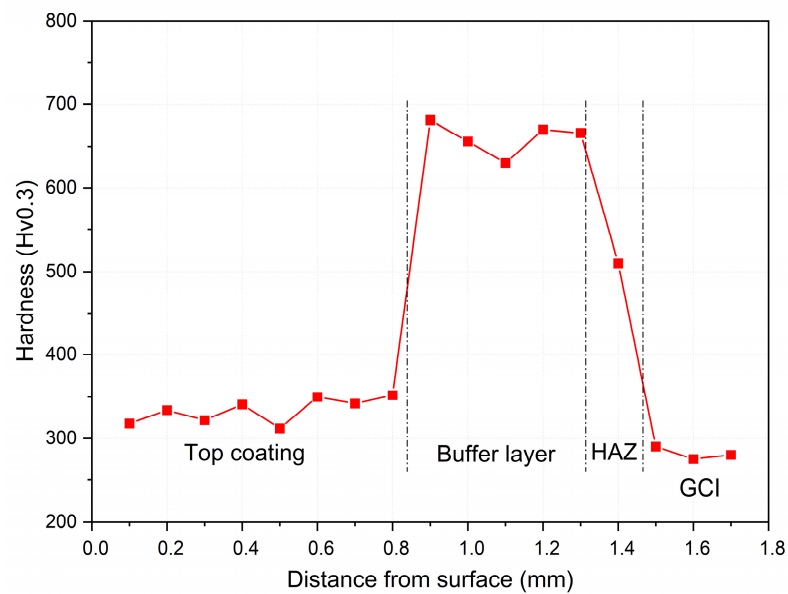**Figure 8.** Hardness profile of the Fe_3Al coating from top to down.
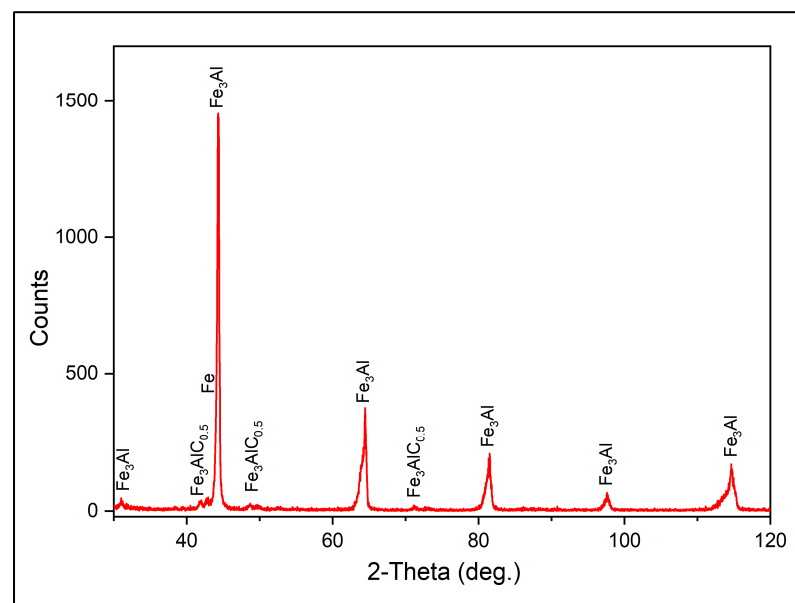

Figure 9. XRD of the Fe_3Al coating on GCI.

The formation of the carbide phase plus the carbon remaining in the solution in the Fe_3Al matrix has a considerable impact on the mechanical properties of iron aluminide alloys, including improvements in the yield strength, creep resistance, and hydrogen-induced cracking resistance [28,29]. Furthermore, recent research has demonstrated that adding carbon to iron aluminides may increase their room-temperature ductility through the formation of perovskite-based $Fe_3AlC_{0.5}$ precipitates in the matrix [30].

3.2. Wear Test Results

Figure 10 shows the trends in the friction coefficient for the Fe_3Al-coated disc, as well as uncoated GCI as a control sample that was compared with the coating. The GCI/Cu-free couple took a longer time to reach a steady state friction coefficient (about 3000 s), whereas the coupling involving the coated disc took place over a relatively short period. The friction coefficient for the GCI/Cu-free and Fe_3Al/ECOPADS sliding couples were approximately

the same at a steady state (0.54). The friction coefficient for the Fe$_3$Al/Cu-free sliding couple reached around 0.57.
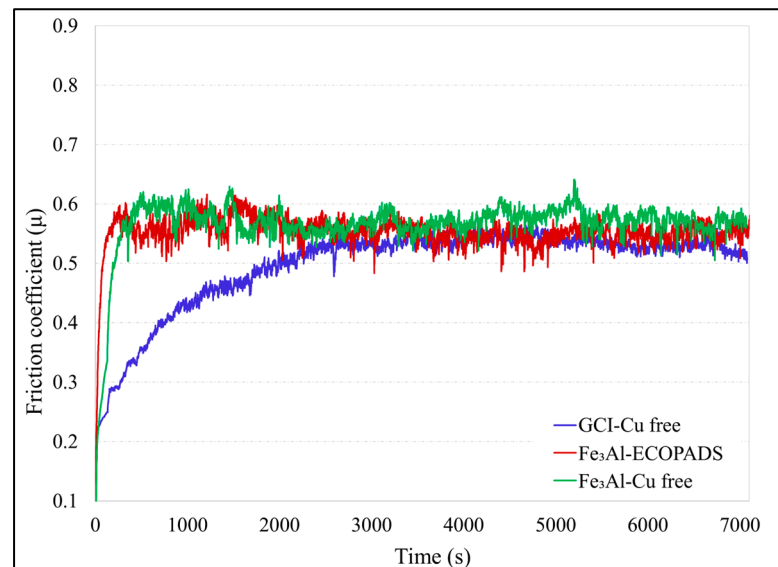

Figure 10. Comparative results for COF of different tribological couplings.

Figure 11 shows the corresponding particulate matter emissions during the pin-on-disc test. The emissions have the same growing tendency as the COF in the case of the uncoated disc, i.e., increasing with an increasing COF during the running-in period before reaching a steady state. Comparing the emissions of different sliding couples, the Fe$_3$Al/Cu-free couple has considerably fewer emissions (476 #/cm^3) than the GCI/Cu-free couple do (600 #/cm^3). The Fe$_3$Al /ECOPADS sliding couple, which takes into account the wear dependency in the composition of the friction material, has even fewer emissions (411 #/cm^3) than the Fe$_3$Al/Cu-free couple does.
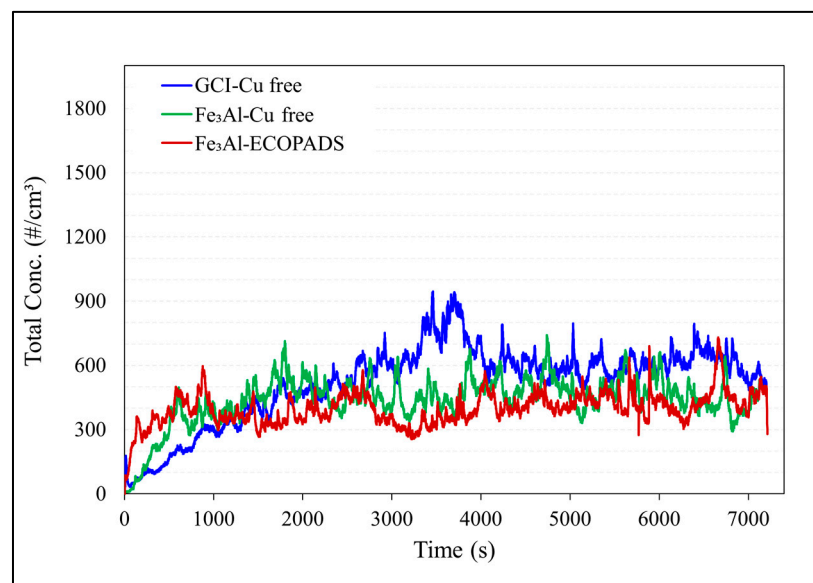

Figure 11. Comparative results for the particulate matter emissions of different tribological couplings.

As stated before, the tribological properties of the Fe$_3$Al coating were investigated in regard to concerns about its wear behavior when sliding against two different friction materials: Cu-free and ECOPADS. The results are presented in Figure 12, which shows

the wear of the pin and counterpart disc under diverse sliding circumstances for all the samples. A comparison of the wear behavior of the coating against Cu-free and ECOPADS friction materials showed that the Fe_3Al/ECOPADS couple has a lower total Ka value than the Cu-free/coating sliding couple does, indicating the better wear resistance of the former. When the coated disc slides against the ECOPADS friction material, the Ka value of the Fe_3Al disc was 2.00×10^{-14} m^2/N, which was slightly lower than that when they slid against Cu-free friction material (2.85×10^{-14} m^2/N). On the other hand, when sliding against Cu-free friction materials, the Ka value of GCI was 2.14×10^{-14} m^2/N, which increased to 2.85×10^{-14} m^2/N when the GCI was replaced with a coated disc (i.e., Fe_3Al/Cu-free sliding pair). Further analysis of the worn surface of the pin and disc will provide an insight into the active mechanisms that caused the observed difference in wear behavior between the coating against the two different friction materials.
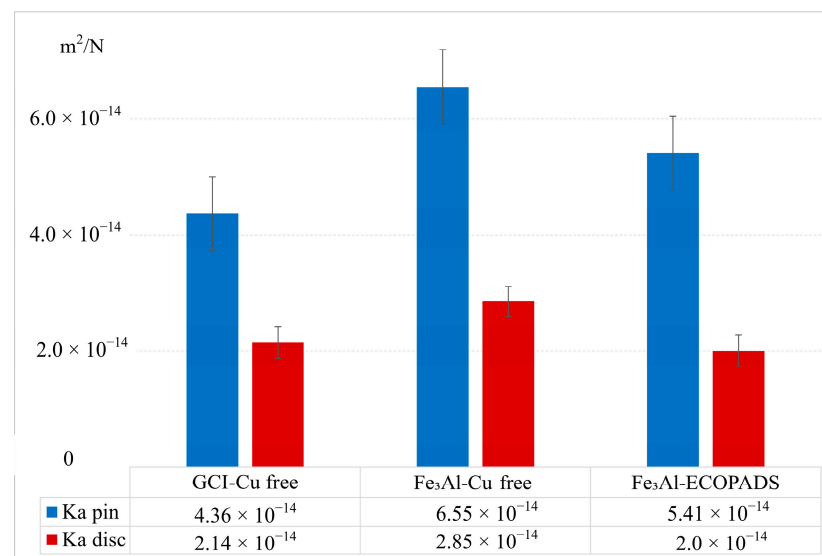

m^2/N	GCI-Cu free	Fe_3Al-Cu free	Fe_3Al-ECOPADS
■ Ka pin	4.36×10^{-14}	6.55×10^{-14}	5.41×10^{-14}
■ Ka disc	2.14×10^{-14}	2.85×10^{-14}	2.0×10^{-14}

Figure 12. Wear rate, Ka, of pin and disc related to the sliding couples.

Figure 13 shows the typical morphologies of the worn surfaces of the pin and related counterpart discs. In this figure, a compacted secondary plateau can be seen to have formed aside the iron fibers, acting as primary plateaus, emerging from the worn pin surface, thus blocking and favoring the compaction of the wear debris. The X-ray maps in Figure 14 show the spatial distribution of the main elements on the worn pin surface, providing interesting clues regarding the contribution of oxides to the formation and extension of secondary plateaus on the surface of the pin.
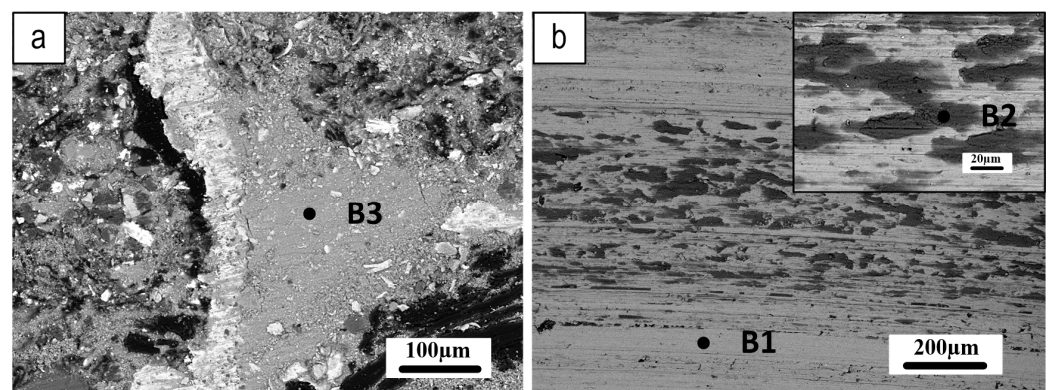

Figure 13. SEM analysis of the Fe_3Al/Cu free sliding couple after PoD test; (**a**) worn pin surface and (**b**) wear track. The spots of the EDXS analyses are indicated (see Table 3 for relevant results).
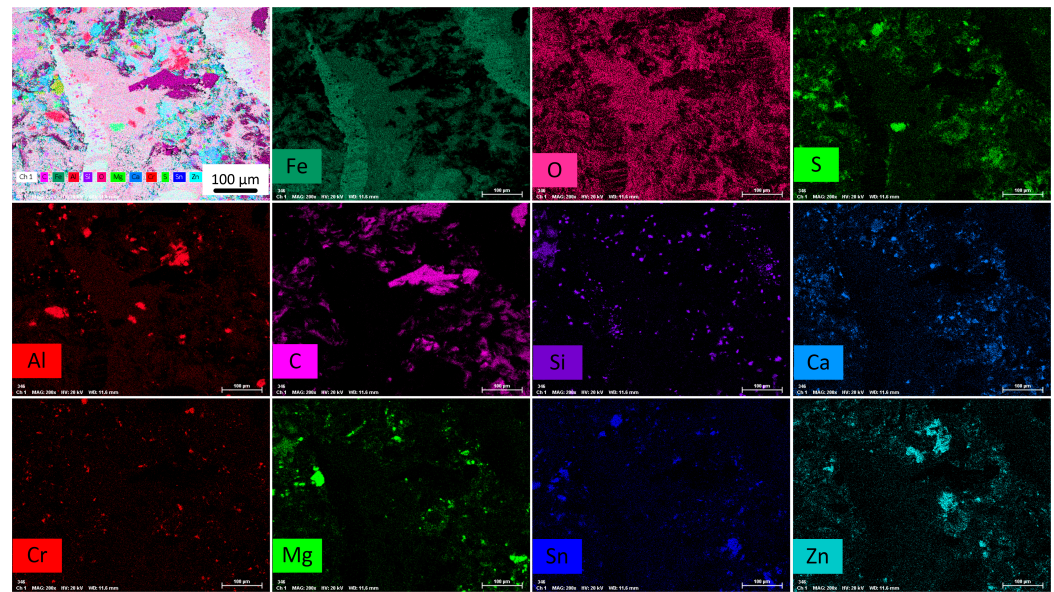
Figure 14. X-ray maps of the Cu-free pin surface for the Fe$_3$Al-coated/Cu-free sliding couple after the pin-on-disc test.

Table 3. EDXS analysis of the points B1, B2, and B3 marked in Figure 13, which are related to the composition of the friction layers which formed on the Fe$_3$Al-coated disc and Cu-free pin after the PoD sliding tests. The carbon concentration was not evaluated.

	B1 (wt.%)	B2 (wt.%)	B3 (wt.%)
O	3	19.3	20.8
Al	11.9	7.9	8.8
Cr	1.0	1.1	0.8
Fe	83.3	57.2	55.9
Mg	0.4	3.9	2.8
Si	0.4	1.5	1.8
Zn	-	3.9	3.8
Sn	-	2.3	2.4
S	-	2.2	2.3
Ca	-	0.7	0.6

Figure 13b shows wear tracks on the Fe$_3$Al-coated disc at two different magnifications. Many grooves can be seen along the sliding direction, indicating the occurrence of abrasion to some extent on the disc. These surface features are typically produced due to abrasion with materials with a higher hardness, such as MgO, Al$_2$O$_3$, and other oxides, which contribute to wear during the PoD test. Additionally, darker gray color patches can be seen on the wear tracks, where most of the transferred material is located.

Table 3 shows the results of the EDXS investigations in three different spots, as indicated in Figure 13, selected as follows: a point of the wear track where there is no sign of transferred materials (B1); patches of the transfer layer on the wear track on the disc (B2); a secondary plateau on the worn pin surface (B3). EDXS analysis confirmed the presence of all the elements from the friction material and a relatively large amount of Fe and Al originating from the Fe$_3$Al coating.

The analyses for the Fe$_3$Al/Cu-free mating couple indicate a high content of iron oxides in the secondary plateaus on the pin surface and transfer layer on the disc. Iron turned out to be always in association with a relatively large amount of Al, originating from the coating.

Figure 15 depicts the etched surface of the coating after the PoD test against the Cu-free friction material. It was observed that the materials transferred from the pad and coating onto the wear track. The $Fe_3AlC_{0.5}$ carbide phase (Figures 5 and 9) was also observed on the etched surface. The microstructure of the coating indicates that plastic deformation occurred at the surface due to sliding contact with friction materials during the PoD test.
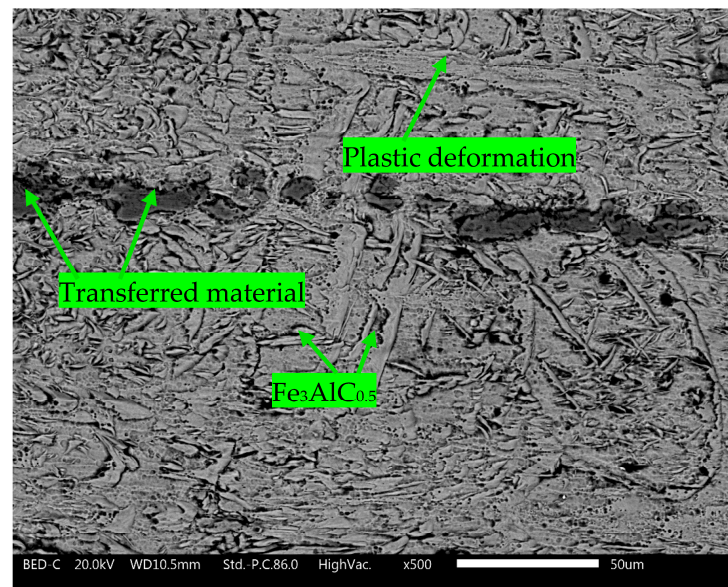

Figure 15. The etched surface of the Fe_3Al coating after PoD test against the Cu-free friction material.

Figure 16 shows SEM micrographs of the worn pin and wear tracks on its counterpart Fe_3Al disc, offering important insights into the tribological behavior of the system. The well-compacted secondary plateaus observed on the worn pin surface (Figure 16a) suggest that the tribo-oxidation mechanism played a role in the wear process. Meanwhile, the parallel scratches and small amount of transferred material observed on the coated disc (Figure 16b) indicate that the abrasion mechanism may have been a significant contributor to wear.
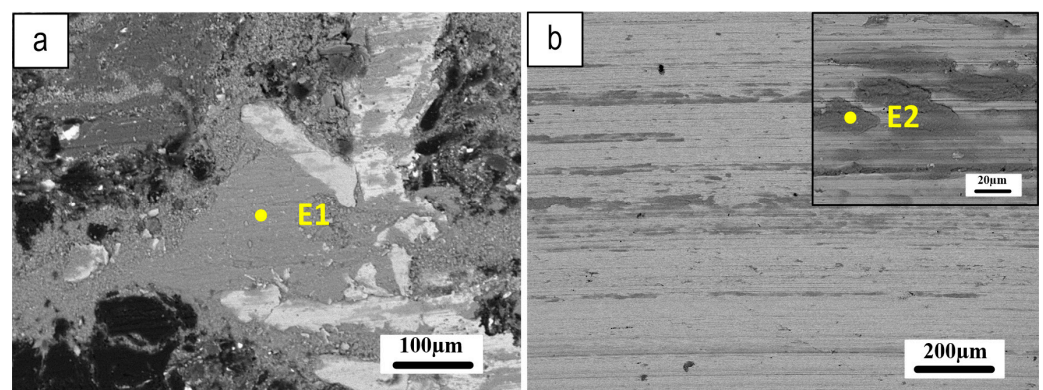

Figure 16. SEM analysis of the Fe_3Al/ECOPADS sliding couple after PoD test; (**a**) worn pin surface and (**b**) wear track.

Table 4 provides the EDXS analysis results of the friction layer on the ECOPADS pin and coated disc, corresponding to the coded points in Figure 16 (E1 and E2, respectively). The elemental compositions reveal contributions from both the pin and coating materials, providing further insight into the underlying mechanisms of the tribological behavior of the system.

Table 4. EDXS analysis of the points (E1 and E2) in Figure 16 related to the friction layer composition formed on the surface of the sliding couples Fe_3Al/ECOPADS. As for the former compositional data, carbon was not quantified.

	E1 (wt.%)	E2 (wt.%)
O	22.6	18.7
Al	7.4	8.5
Cr	0.8	0.7
Fe	52.1	51.2
Ba	6.4	7.0
Mg	2.3	2.7
Si	1	1.0
Zn	2.2	3.2
Sn	1.5	2.1
S	3.1	3.7
Ca	0.6	0.8

In both cases, whether Cu-free or ECOPADS friction materials were used, the formation and extension of secondary plateaus on the surface of the pins were observed (Figures 13a and 16a). These compacted secondary plateaus play a role in providing efficient contact in the interface area, leading to a more consistent and stable friction coefficient. Furthermore, the extension of secondary plateaus on the pin surface facilitates the smooth movement of the sliding bodies [31]. The transferred materials on the coated disc surface also appear to influence the wear behavior [13]. In the case of Cu-free friction materials, a higher amount of Fe was observed in the secondary plateaus and transferred materials onto the disc, which is known to be present on the pad and coating (Figures 13, 15 and 16).

According to a study conducted by Olofsson et al. [13], in the recycling of brake discs using a stainless steel coating, there is a noticeable tendency for materials to transfer onto the disc during the PoD test. This transfer of materials was found to have an adverse effect on the friction coefficient and emissions. Additionally, this resulted in a higher weight loss for both the pin and the disc, which exceeded that of the uncoated GCI disc. For the Fe_3Al coating, the increased Fe content also seemed to enhance adhesive wear by slightly increasing the coefficient of friction. However, the wear results were comparable to those of the uncoated GCI disc.

Figure 17 shows SEM micrographs of the worn pin and wear tracks associated with the GCI/Cu-free sliding couple. Compacted and extended secondary plateaus are observed behind the iron fibers on the surface of the Cu-free pin (Figure 17a), and minor materials transferred to the wear track (Figure 17b). In the wear track on the GCI disc, several grooves running in the sliding direction indicate the abrasive wear mechanism occurring in the GCI disc. The GCI/Cu-free pairing (Figure 17) has a relatively high amount of Fe oxides on the secondary plateaus as well as on the transferred materials (see items F1 and F2 in Table 5), which confirms the contribution of the tribo-oxidation mechanism in the system. This is consistent with the observed low friction coefficient in this scenario. In the case of the Fe_3Al coating, the Fe content decreases, while the Al content originating from the coating takes its place.
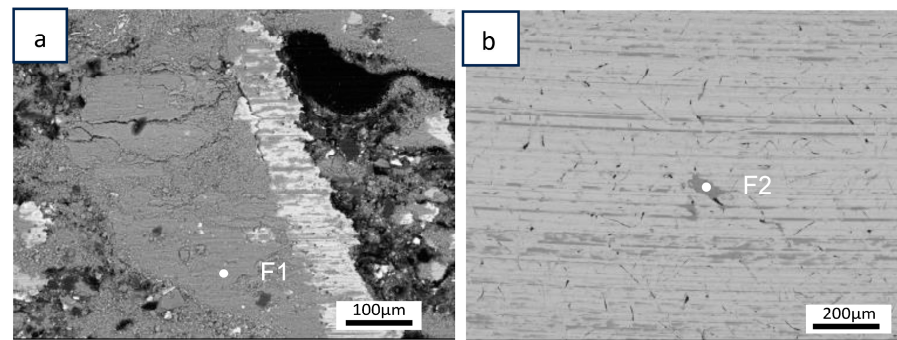
Figure 17. SEM analysis of the GCI/Cu free sliding couple after PoD test; (**a**) worn pin surface and (**b**) wear track.

Table 5. EDXS analysis of the points (F1 and F2) in Figure 17 related to the friction layer composition formed on the surface of the GCI/Cu-free sliding couples. As for the former compositional data, carbon was not quantified.

	F1 (wt.%)	F2 (wt.%)
O	28	26.8
Al	1.4	1.3
Cr	0.4	0.6
Fe	61	62.3
Mg	1.7	1.8
Si	1.4	1.4
Zn	2.5	2
Sn	1.4	1.6
S	1.3	1.3
Ca	0.4	0.4
Mn	0.5	0.5

The particles that are released into the PoD chamber can offer valuable insights into the mechanisms of formation and disruption of the friction layer. Figure 17 presents the EDXS semi-quantitative chemical analysis of the particles emitted from the Fe_3Al coating/ECOPADS sliding couple and picked up from the inner walls of the PoD chamber. The full-frame EDXS analysis of the particles (Figure 18a) indicates that their chemical composition is typical of the transfer layer on the worn track and secondary plateaus generated on the pin surface (as shown in Table 3). Moreover, the EDXS analysis of a randomly selected large particle (Figure 18b) that settled inside the chamber revealed high concentrations of Ba, S, and O. This composition is consistent with barium sulfate, which is a typical ingredient of the ECOPADS friction material (see Table 2). Regarding the size of the particles released from the system (Figure 18), larger particulate matter is less harmful to human health than smaller particles is [32]. This is because larger particles, if still airborne, tend to be filtered out by the upper part of the respiratory system, whereas smaller particles can penetrate deeper into the lungs and even enter the bloodstream.
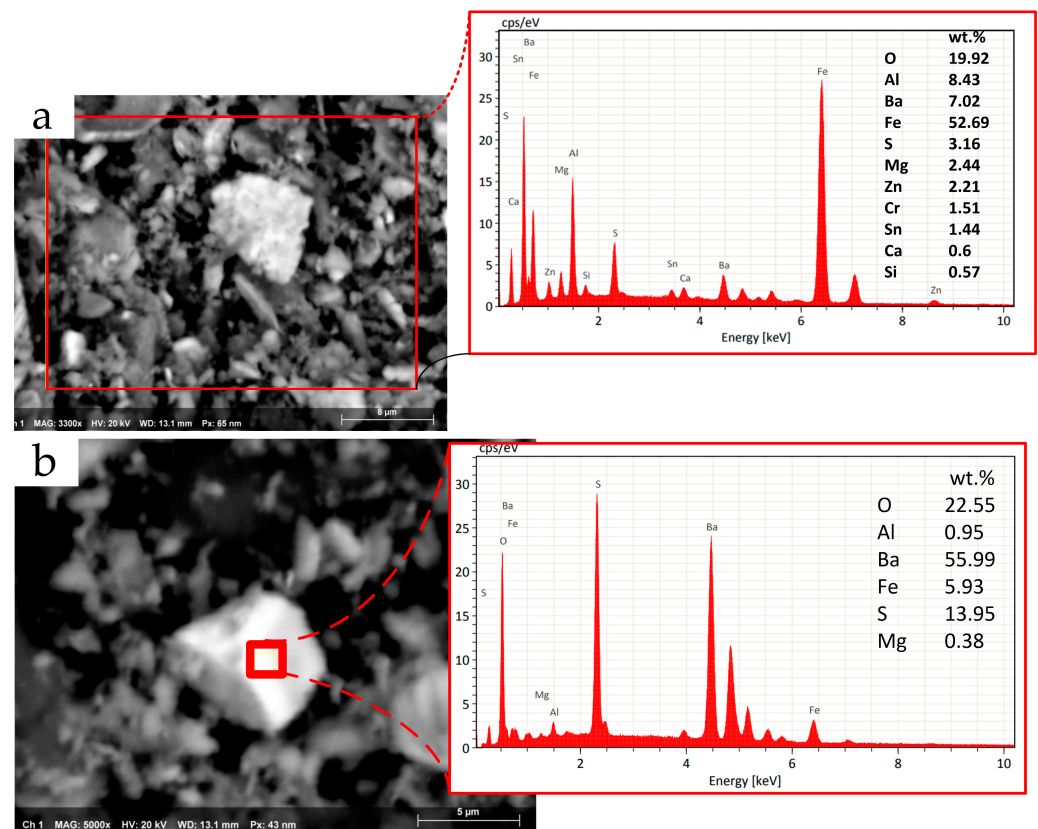
Figure 18. (**a**) SEM and EDXS analyses of the particles collected from the PoD enclosure chamber. (**b**) EDXS analysis of a typical relatively large particle retrieved inside the enclosure chamber of the PoD test rig.

4. Conclusions

The comprehensive analysis presented in this study provides important insights that highlight the application of Fe_3Al coating as an environmentally friendly substitute for coatings containing critical elements for GCI brake discs to mitigate the environmental concerns associated with brake systems.

The microstructure of the Fe_3Al coating reveals the presence of finely dispersed needle-like $Fe_3AlC_{0.5}$ carbides embedded within the alloy grains. These microstructural characteristics influence the tribological performance of the coated disc.

The coating/ECOPADS friction material tribological couple exhibits a reduced wear rate compared to that of the coating/Cu-free sliding couple, underlining better wear resistance in the former configuration.

While the wear results indicated a coefficient of friction similar to that of an uncoated disc (approximately 0.55), the coating/Cu-free sliding couple shows substantially reduced PM emissions compared to those of the GCI/Cu-free pairing, dropping from 600 to 476 #/cm^3. Particularly, even further reductions in PM emissions are achieved with the coating/ECOPADS sliding coupling (411 #/cm^3), underlining the advantageous environmental aspect of the Fe_3Al coating.

Author Contributions: Conceptualization, H.R. and C.M.; methodology, H.R, S.G., C.M. and G.S.; formal analysis, H.R.; investigation, H.R. and S.A.; resources, S.A.; writing—original draft preparation, H.R. and C.M.; writing—review and editing, H.R., S.G., C.M., G.S. and S.A.; supervision, S.G. and G.S. All authors have read and agreed to the published version of the manuscript.

Data Availability Statement: The data presented in this study are available on request from the corresponding author.

Conflicts of Interest: The authors declare no conflict of interest.

References

1. Lyu, Y.; Leonardi, M.; Mancini, A.; Wahlström, J.; Olofsson, U. Tribology and Airborne Particle Emission of Laser-Cladded Fe-Based Coatings versus Non-Asbestos Organic and Low-Metallic Brake Materials. *Metals* **2021**, *11*, 1703. [CrossRef]
2. Aranke, O.; Algenaid, W.; Awe, S.; Joshi, S. Coatings for Automotive Gray Cast Iron Brake Discs: A Review. *Coatings* **2019**, *9*, 552. [CrossRef]
3. Verma, P.C.; Alemani, M.; Gialanella, S.; Lutterotti, L.; Olofsson, U.; Straffelini, G. Wear debris from brake system materials: A multi-analytical characterization approach. *Tribol. Int.* **2016**, *94*, 249–259. [CrossRef]
4. Zhang, Q.; Lu, D.; Wang, D.; Yang, X.; Zuo, P.; Yang, H.; Fu, Q.; Liu, Q.; Jiang, G. Separation and Tracing of Anthropogenic Magnetite Nanoparticles in the Urban Atmosphere. *Environ. Sci. Technol.* **2020**, *54*, 9274–9284. [CrossRef]
5. Ciudin, R.; Verma, P.C.; Gialanella, S.; Straffelini, G. Wear debris materials from brake systems: Environmental and health issues. *WIT Trans. Ecol. Environ.* **2014**, *191*, 1423–1434. [CrossRef]
6. Li, W.; Yang, X.; Wang, S.; Xiao, J.; Hou, Q. Comprehensive Analysis on the Performance and Material of Automobile Brake Discs. *Metals* **2020**, *10*, 377. [CrossRef]
7. Opel, T.; Langhof, N.; Krenkel, W.; Krenkel, I.W. Development and tribological studies of a novel metal-ceramic hybrid brake disc. *Int. J. Appl. Ceram. Technol.* **2022**, *19*, 62–74. [CrossRef]
8. Goo, B.-C. Development and Characterization of C/C-SiC Brake Disc. *Mater. Manuf. Process.* **2016**, *31*, 979–988. [CrossRef]
9. Rajaei, H.; Menapace, C.; Amirabdollahian, S.; Perini, M.; Straffelini, G.; Gialanella, S. Microstructural and Tribological Evaluation of Brake Disc Refurbishing Using Fe-Based Coating via Directed Energy Deposition. *Metals* **2022**, *12*, 465. [CrossRef]
10. Shamanian, M.; Abarghouie, S.M.; Pour, S.M. Effects of surface alloying on microstructure and wear behavior of ductile iron. *Mater. Des.* **2010**, *31*, 2760–2766. [CrossRef]
11. Chioibasu, D.; Mihai, S.; Cotrut, C.M.; Voiculescu, I.; Popescu, A.C. Tribology and corrosion behavior of gray cast iron brake discs coated with Inconel 718 by direct energy deposition. *Int. J. Adv. Manuf. Technol.* **2022**, *121*, 5091–5107. [CrossRef]
12. Kılıç, H.; Mısırlı, C.; Mutlu, I.; Timur, M. Mechanical and tribological properties of a WC-based HVOF spray coated brake disc. *Mater. Test.* **2022**, *64*, 1150–1161. [CrossRef]
13. Olofsson, U.; Lyu, Y.; Åström, A.H.; Wahlström, J.; Dizdar, S.; Nogueira, A.P.G.; Gialanella, S. Laser Cladding Treatment for Refurbishing Disc Brake Rotors: Environmental and Tribological Analysis. *Tribol. Lett.* **2021**, *69*, 57. [CrossRef]
14. Rettig, M.; Grochowicz, J.; Käsgen, K.; Eaton, R.; Wank, A.; Hitzek, A.; Schmengler, C.; Koss, S.; Voshage, M.; Verpoort, C.; et al. Carbidic Brake Rotor Surface Coating Applied by High-performance-laser Cladding. In Proceedings of the Euro Brake 2020, Online, 16–19 June 2020. [CrossRef]
15. Dizdar, S.; Lyu, Y.; Lampa, C.; Olofsson, U. Grey Cast Iron Brake Discs Laser Cladded with Nickel-Tungsten Carbide—Friction, Wear and Airborne Wear Particle Emission. *Atmosphere* **2020**, *11*, 621. [CrossRef]
16. Bastian, S.; Busch, W.; Kühnel, D.; Springer, A.; Meißner, T.; Holke, R.; Scholz, S.; Iwe, M.; Pompe, W.; Gelinsky, M.; et al. Toxicity of Tungsten Carbide and Cobalt-Doped Tungsten Carbide Nanoparticles in Mammalian Cells in Vitro. *Environ. Heal. Perspect.* **2009**, *117*, 530–536. [CrossRef]
17. US National Toxicology Program (NTP). Available online: https://ntp.niehs.nih.gov/ (accessed on 17 May 2023).
18. European Chemical Agency. Available online: https://echa.europa.eu/home (accessed on 17 May 2023).
19. Liu, Z.; Han, Q.; Guo, Y.; Lang, J.; Shi, D.; Zhang, Y.; Huang, Q.; Deng, H.; Gao, F.; Sun, B.; et al. Development of interatomic potentials for Fe-Cr-Al alloy with the particle swarm optimization method. *J. Alloy. Compd.* **2019**, *780*, 881–887. [CrossRef]
20. Mulyawan, A.; Terai, T.; Fukuda, T. Interpretation of Fe-rich part of Fe–Al phase diagram from magnetic properties of A2-, B2-, and DO3-phases. *J. Alloy. Compd.* **2020**, *834*, 155140. [CrossRef]
21. Luo, X.; Zhang, K.; Cao, J.; Meng, G.; Yu, F.; Zhou, Y.; Zhou, H.; La, P.; Xie, H. Effect of line energy density of the laser beam on the microstructure and wear resistance properties of the obtained Fe_3Al laser cladding coatings. *Optik* **2022**, *261*, 169256. [CrossRef]
22. Alman, D.E.; Hawk, J.A.; Tylczak, J.H.; Doğan, C.P.; Wilson, R.D. Wear of iron-aluminide intermetallic-based alloys and composites by hard particles. *Wear* **2001**, *251*, 875–884. [CrossRef]
23. Menapace, C.; Leonardi, M.; Matějka, V.; Gialanella, S.; Straffelini, G. Dry sliding behavior and friction layer formation in copper-free barite containing friction materials. *Wear* **2018**, *398–399*, 191–200. [CrossRef]
24. Grum, J.; Šturm, R. Comparison of measured and calculated thickness of martensite and ledeburite shells around graphite nodules in the hardened layer of nodular iron after laser surface remelting. *Appl. Surf. Sci.* **2002**, *187*, 116–123. [CrossRef]
25. McKamey, C.; Liu, C. Chromium addition and environmental embrittlement in Fe_3Al. *Scr. Met. Et Mater.* **1990**, *24*, 2119–2122. [CrossRef]
26. Deevi, S.C. Advanced intermetallic iron aluminide coatings for high temperature applications. *Prog. Mater. Sci.* **2021**, *118*, 100769. [CrossRef]
27. Johansson, P.; Uhrenius, B.; Wilson, A.; Ståhlberg, U. Processing, Fabrication, and Mechanical Properties of Fe_3Al Based PM Alloys. *Powder Met.* **1996**, *39*, 53–58. [CrossRef]

28. Parvathavarthini, N.; Prakash, U.; Dayal, R. Effect of carbon addition on hydrogen permeation in an Fe$_3$Al-based intermetallic alloy. *Intermetallics* **2002**, *10*, 329–332. [CrossRef]

29. Sundar, R.S.; Deevi, S.C. Effect of carbon addition on the strength and creep resistance of FeAl alloys. *Metall Mater Trans A Phys Metall Mater Sci* **2003**, *34*, 2233–2246. [CrossRef]

30. Zhu, S.M.; Guan, X.S.; Shibata, K.; Iwasaki, K. Effect of carbon addition on tribological properties of Fe-Al alloys. *Metall. Mater. Trans. A Phys. Metall. Mater. Sci.* **2002**, *33*, 1292–1295. [CrossRef]

31. Cho, M.H.; Cho, K.H.; Kim, S.J.; Kim, D.H.; Jang, H. The Role of Transfer Layers on Friction Characteristics in the Sliding Interface between Friction Materials against Gray Iron Brake Disks. *Tribol. Lett.* **2005**, *20*, 101–108. [CrossRef]

32. Franck, U.; Odeh, S.; Wiedensohler, A.; Wehner, B.; Herbarth, O. The effect of particle size on cardiovascular disorders—The smaller the worse. *Sci. Total. Environ.* **2011**, *409*, 4217–4221. [CrossRef]